Mycn regulates intestinal development through ribosomal biogenesis in a zebrafish model of Feingold syndrome 1

Yun-Fei Li[1#], Tao Cheng[1#], Ying-Jie Zhang[1], Ying Huang[1], Xiao-Zhi Sun[1], Dan Wang[1], Xiang Liu[1] Dong Chen[3], Xi Jin[4*], Peng-Fei Xu[1, 2*]

[1]Institute of Genetics and Department of Human Genetics, Zhejiang University School of Medicine, Hangzhou, China.
[2]Women's Hospital, Zhejiang University School of Medicine, Hangzhou, China.
[3]Department of Colorectal Surgery, The First Affiliated Hospital, Zhejiang University School of Medicine, Hangzhou 310003, Zhejiang Province, China.
[4]Department of Gastroenterology, The First Affiliated Hospital of Zhejiang University School of Medicine, No. 79, Qingchun Road, Hangzhou, China.
*Correspondence: jxfl007@zju.edu.cn, pengfei_xu@zju.edu.cn
#Yun-Fei Li and Tao Cheng contributed equally to this article and should be regarded as joint first authors.

Abstract

Feingold syndrome type 1, caused by loss-of-function of MYCN, is characterized by varied phenotypes including esophageal and duodenal atresia. However, no adequate model exists for studying the syndrome's pathological or molecular mechanisms, nor is there a treatment strategy. Here, we developed a zebrafish Feingold syndrome type 1 model with nonfunctional *mycn*, which had severe intestinal atresia. Single-cell RNA-seq identified a subcluster of intestinal cells was highly sensitive to Mycn, and impaired cell proliferation decreased the overall number of intestinal cells in the *mycn* mutant fish. Bulk RNA-seq and metabolomic analysis showed that expression of ribosomal genes was downregulated and amino acid metabolism was abnormal. Ribosomal profiling analysis showed decreases in free 40S, 60S, and 80S ribosome particles, which led to impaired translation in the mutant. Further, both L-leucine and Rheb, which can elevate translation via TOR pathway, rescued the intestinal phenotype of *mycn* mutant. In summary, by this zebrafish Feingold syndrome type 1 model, we found that disturbance of ribosomal biogenesis and blockage of protein synthesis during development are primary causes of the intestinal defect in Feingold syndrome type 1. Importantly, our work suggests that leucine supplementation may be a feasible and easy treatment option for this disease.

Introduction

Feingold syndrome is a skeletal dysplasia caused by loss-of-function mutations of either MYCN (type 1) or MIR17HG (type 2) which encodes miR-17-92 microRNAs [1]. The syndrome is characterized by autosomal dominant inheritance of microcephaly and limb malformations, notably hypoplastic thumbs, and clinodactyly of the second and fifth fingers. Feingold syndrome type 1 is always accompanied by gastrointestinal atresia (primarily esophageal and/or duodenal atresia) [2]. However, whether the digestive system deficiency in Feingold syndrome 1 is the direct result of MYCN loss of function or a sequence effect of other developmental defects caused by MYCN mutation remains unknown. Further, the mechanism of the intestinal defects in patients with Feingold syndrome type 1 is also unclear. This unclear pathogenesis of Feingold syndrome type 1 is a major obstacle to developing treatments for the disease.

The MYC proto-oncogene family is a class of transcription factors with a basic helix-loop-helix domain and includes MYC, MYCL, and MYCN [3]. MYCN amplification or overexpression has been described in many cancers, including neuroblastoma, retinoblastoma, rhabdomyosarcoma, and lung cancer, which are frequently of

embryonic or neuroendocrine origin [4]. Like other members of the MYC family, MYCN controls the expression of its target genes and regulates many fundamental cellular processes such as proliferation, differentiation, apoptosis, protein synthesis, and metabolism [5]. Research on chicken embryos has shown that overexpression of MYCN drives the neural crest towards a neural stem cell fate [6]. MYCN homozygous mutant mice die at embryonic day E11.5, and multiple organs, including the nervous system, mesonephros, lungs and gut, are affected [7]. Conditional disruption of MYCN in mouse neural progenitor cells has shown that MYCN is essential for neural progenitor cell expansion and inhibits its differentiation [8]. However, the function of MYCN in organogenesis remains uncertain, and the mechanism through which MYCN regulates intestinal development remains unknown.

The vertebrate alimentary canal is derived from the primitive gut tube, which originates from the endodermal layer [9] and gives rise to the digestive system organs, including the pancreas, liver, gall bladder, and intestines. Developmental defects in this process can lead to serious human diseases, such as intestinal atresia, malrotation, hypoplasia, and epithelial defects, which cause malabsorptive or secretory diarrheal syndromes [10]. Although the zebrafish digestive system differs morphologically from that of mammals, a high degree of homology exists between zebrafish intestines and mammalian intestines in terms of their cellular composition and molecular pathways regulating intestinal development [11]. Many zebrafish models for studying congenital diseases affecting the intestines have been reported because of experimental tractability; these models have provided novel insights into the developmental mechanisms, pathogenesis, and therapeutics of intestinal congenital diseases [12-13].

In this study, we generated a large deletion in *mycn* in zebrafish using the CRISPR/Cas9 system. Homozygous *mycn* mutant fish are viable and fertile, and most importantly, the mutants carry a series of developmental defects similar to those of Feingold syndrome type 1, such as an abnormal pharyngeal arch (cartilage defects) and intestinal deficiency. Using this model, we studied the mechanism of the Mycn deficiency leading to intestinal developmental defects and discovered a potential therapeutic strategy for alleviating the intestinal defects in patients with Feingold syndrome type 1.

Results

mycn was highly enriched in the developing digestive system of the zebrafish embryos

To use zebrafish as a model for studying Feingold syndrome type 1 and the function of Mycn during organogenesis, we first explored the spatiotemporal expression patterns of *mycn* during embryonic development in zebrafish. *mycn* transcription can be detected by RNA *in situ* hybridization at the onset of gastrulation and is enriched in the neural ectoderm. At the end of gastrulation, *mycn* was specifically expressed in both the anterior and posterior neural plate, consistent with previous reports on the role of MYCN in neural development and oncogenesis [24]. Beginning at 18 hpf, *mycn* expression could be detected in the epiphysis, eye, optic tectum, spinal cord, and endoderm (Fig. S1A). After 24 hpf, *mycn* expression was progressively restricted to the central nervous system, pharyngeal arch, and digestive system (Fig. 1A).

To validate the *in situ* hybridization results and investigate the *mycn* expression dynamics during zebrafish development, we generated an *mycn:EGFP* knockin fish by inserting an EGFP sequence just before the stop codon of *mycn* with a P2A linker between the two proteins (Fig S1C) to avoid possibly distorting the Mycn

protein structure. The *mycn:EGFP* line confirmed that *mycn* was mainly expressed in the central nervous and digestive systems during organogenesis (Fig. 1C). Interestingly, *mycn* was also expressed in the migrating neuromast cells of the lateral line, indicating that Mycn might also function in the sensory organs. High-magnification imaging of both the *mycn in situ* hybridization and *mycn:EGFP* showed that *mycn* was expressed in the intestinal epithelial cells, suggesting that Mycn functions directly in intestinal development (Fig. 1B, D).

To further characterize the *mycn* expression pattern, we performed single-cell RNA-seq for WT embryos at 3 dpf. 23 clusters were identified and annotated after strict quality control (Fig. 1E). We then explored the *mycn* expression level across these clusters and found that *mycn* was highly expressed in the central nervous system, neural crest cells, and endoderm-derived tissues such as the intestines, liver, and pancreas (Fig. 1F). Additionally, we investigated *mycn* expression in published single-cell RNA-seq datasets [25-27]. During the gastrulation and somitogenesis stages, the brain and optic cells showed high *mycn* expression (Fig. S1 D, E). High *mycn* expression levels were detected in intestinal cells at 2 dpf, and *mycn* expression decreased in the intestines at 5 dpf (Fig. S1B, F-I), which was consistent with the *in situ* hybridization (ISH) experiment on *mycn*.

mycn mutation results to multiple developmental defects in zebrafish recapitulating human Feingold syndrome type1

To construct a zebrafish model of Feingold syndrome and study the function of Mycn during development, we generated a *mycn* mutant fish line using the CRISPR-Cas9 system. Three gRNAs targeting exon2 of *mycn* were injected together with Cas9 into zebrafish embryos at the 1-cell stage, resulting in a 308-bp deletion in the CDS (coding sequence) of *mycn* (Fig. S2A). This large deletion was easily discriminated via PCR and led to early termination of the Mycn protein (122 amino acids left) (Fig. S2B). Surprisingly, some of the homozygous *mycn* mutant fish survived to adulthood and were fertile.

The WT and *mycn* mutant zebrafish did not noticeably differ morphologically(Fig. S8A-C) until 4 dpf; at this stage, the *mycn* mutants lacked swim bladder, and their heads and eyes were smaller than those of the WT fish(Fig. S8D, E) , but those defects become less obvious after 1 day of development in some of the mutants (Fig. 2A). Alcian blue staining showed that the pharyngeal arch, was severely malformed in most of the 5 dpf *mycn* mutants (Fig. 2B). This phenotype mimics the maxillofacial deformity that is frequently observed in Feingold syndrome.

Gastrointestinal atresia is another of the most distinctive yet least studied symptoms of Feingold syndrome type 1. The highly enriched expression of *mycn* mRNA in the developing intestines of zebrafish suggests that Mycn has a direct function in intestinal development. To investigate this, we firstly crossed our *mycn* mutant fish with a gut epithelial reporter *ET33J1: EGFP* zebrafish line [28]. The reporter showed that the size of the entire intestine of the *mycn* mutants at 5 dpf was dramatically smaller than that of the WT fish (Fig. 2C). DCFH-DA treatment at 7 dpf also confirmed the intestinal developmental defect in the *mycn* mutants (Fig. 2D). HE staining of the intestinal sagittal section showed that in the anterior region of the *mycn* mutant intestine (intestinal bulb), the intestinal folds were obviously smaller and fewer, the mid and posterior intestines of the *mycn* mutants showed an obviously narrowed lumen, and the goblet cells, which emerge in the middle of the intestines, could hardly be detected. Conversely, the goblet cells in the WT fish could be easily detected at 4 dpf (Fig. 2G). Whole mount ISH (WISH) results also showed that expression of the intestinal marker, intestine fatty acid-binding protein (*ifabp*), was drastically reduced, likely due to the reduced intestinal size (Fig. 2E).

To verify that *mycn* loss of function, rather than off-target effects, caused these phenotypes, we performed a rescue experiment in the *mycn* mutant embryos by injecting a plasmid with the full-length *mycn* and an EGFP sequence under the *sox17* promoter. The *sox17-mycn* cassette was flanked by tol2 transposons, and transposase mRNA was co-injected to improve the expression efficiency. The intestinal size was significantly restored in the embryos that had strong endodermal EGFP expression, as shown by the *ifabp* expression (Fig. 2F). These results confirmed that the intestinal defects in the mutant fish resulted from the loss of function of Mycn and suggest that Mycn functions directly in endoderm development.

In addition to the intestines, the primitive gut tube (foregut) gives rise to the liver and pancreas. Thus, we performed WISH using markers of the liver (*lfabp*), the exocrine pancreas (*prss1*), and islets (*insulin*) in the WT and *mycn* mutant embryos at 3 dpf. The *mycn* mutants displayed a smaller liver and exocrine pancreas, while islet development appeared unaffected (Fig. S3A). To trace the earliest discernable stage of the endoderm phenotypes in the *mycn* mutants, we performed WISH using the pan-endodermal markers *foxa1*, *foxa3* and *gata6* in embryos at 30 and 48 hpf. At 30 hpf, when the liver and pancreas buds began to emerge, these markers did not obviously differ between the WT and *mycn* mutant embryos. This suggests that Mycn loss-of-function did not strongly affect differentiation of the liver and pancreas during their budding stages. However, the smaller liver, pancreas, and intestines at 48 hpf indicated that Mycn plays an important role during outgrowth of these digestive organs (Fig. S3B).

To further analyze the functional defects in the digestive tracts of the *mycn* mutants, we treated the embryos with PED6 (for lipid-processing activity) or EnzChek (for protein-processing activity) (Fig. S4A) [29]. Although these activities were severely compromised overall, the fluorescence intensity appeared normal in the mutants, suggesting that although the mutant intestinal morphology was highly defective, its main absorption and digestive functions were not completely lost. Thus, we further analyzed the three main functional cells of the intestines: the absorptive, enteroendocrine, and goblet cells [30]. Periodic acid-Schiff and Alcian blue staining of the sagittal sections indicated that goblet cells was dramatically reduced but could still be observed in the *mycn* mutants at 5 dpf (Fig. S4B). HE staining also confirmed this (Fig. 2G). For the enteroendocrine and absorptive cells, we performed WISH using *pyyb* (enteroendocrine cell marker) and *slc15a1b* (absorptive cell marker) probes. Although both could be detected, expression of these markers was dramatically decreased in the *mycn* mutants (Fig. S4C). In summary, Mycn loss-of-function led to abnormal development of the entire digestive tract. Although differentiation of the main functional cells was unaffected, Mycn loss-of-function caused a decrease in the overall intestinal size and further weakened the digestive system functions.

In addition to the endodermal defects, the enteric neurons were significantly reduced in the mutants compared with those of the WT fish at 5 dpf, in terms of both fluorescence intensity and cell numbers, as demonstrated by the anti-HuC antibody (Fig. S4D). Whether this phenotype was due to the direct loss-of-function of Mycn in the enteric neuron or was a sequence effect of the intestinal atresia should be further investigated.

Single-cell transcriptomics showed that Mycn loss-of-function reduced the specific intestinal cell types during embryonic development

To systematically investigate the phenotypes resulting from Mycn loss-of-function at a higher resolution, we performed single-cell RNA-seq in the *mycn* mutant fish at 3 dpf. We integrated *mycn* mutant scRNA-seq datasets with WT datasets (see Methods). 27 cell types were identified and annotated based on their expression

markers (Fig. 3A and S5A). Calculating the cell ratio of each cell type revealed that the cranial neural crest, blood vessels, and digestive organs, including the intestines, liver, and pancreas, were dramatically decreased in the *mycn* mutants (Fig. 3B). To more deeply characterize the intestinal cell clusters, we selected and reclustered the intestinal cells and identified 9 subclusters (Fig. 3C). We noticed that cluster 8 highly expressed *mycn*, and this cluster showed stemness characteristics based on the pseudotime trajectory analysis (Fig. S5C, D), this cluster was completely disappeared in the *mycn* mutants. Besides, clusters 4 and 6 were significantly reduced in the *mycn* mutant. To characterize these subclusters, we performed differential expression analysis, selected the most significant markers (Fig. 3D), and verified their expressions via ISH in both WT and *mycn* mutant embryos. Expressions of all those selected cluster markers were decreased in the *mycn* mutant intestines at 3 dpf, especially for those of clusters 4, 6, 7, and 8, which could hardly be detected in the mutants (Fig. 3E).

Proliferation arrest, but not apoptosis, led to intestinal defects in the mycn mutants

The morphological, molecular, and single-cell RNA-seq results indicated that the intestinal defects in the *mycn* mutants may be due to reduced cell numbers rather than to a differentiation blockade. Thus, we analyzed the levels of proliferation and apoptosis in the intestines of the *mycn* mutant and WT embryos at 3 dpf. Immunofluorescence showed that the PCNA signals were significantly reduced in the intestinal bulbs of the *mycn* mutants (Fig. 4A, Fig. S9). However, TUNEL assay revealed no obvious apoptotic signals in the intestinal bulb region of either the *mycn* mutant or WT embryos (Fig. 4B). To further confirm the intestinal proliferation defects of the *mycn* mutants, we dissociated the 3 dpf embryos of the *mycn*−/−; *ET33J1: EGFP* line and performed fluorescence activated cell sorting to sort out the intestinal cells. We then used BrdU and Annexin V-APC analysis to mark the cells that were proliferating or undergoing apoptosis, respectively. Consistent with the immunofluorescence results, the flow cytometry results also showed a significantly lower proliferation rate in the *mycn* mutants, but apoptosis could hardly be detected in the intestines of either the WT or mutant embryos at 3 dpf (Fig. 4C-E).

Protein translation and nucleotide biosynthesis were compromised in the mycn mutants

To understand the molecular mechanism of the decreased proliferation that led to intestinal developmental defects in the *mycn* mutants, we performed bulk RNA-seq in the *mycn* mutant and WT embryos at 2 and 3 dpf. Compared with the WT fish, we identified 470 down-regulated and 287 up-regulated genes in 2 dpf *mycn* mutants, 451 down-regulated genes and 409 up-regulated genes in 3 dpf *mycn* mutants, respectively (Fig. 5A and Fig. S6A, B). Among them, 85 genes were down-regulated in both stages (Fig. 5A). Gene ontology (GO) enrichment analysis revealed that these 85 genes were mainly involved in the processes of ribosomal assembly, translation, nucleotide/nucleoside biosynthesis, and nucleoside metabolism (Fig. 5B, D). Interestingly, interaction networks of enriched GO terms revealed that the digestive system development, including that of the pancreas, was closely related to the ribosomal assembly/biogenesis (Fig. S6C). Surprisingly, among the 85 down-regulated genes, most of those related to ribosomal assembly were found in previously published MYCN ChIP-seq data on mouse embryonic stem cells (ESC) [31], strongly suggesting that these genes are direct targets of Mycn in zebrafish (Fig. 5C). qPCR analysis further confirmed the down-regulation of those ribosomal genes in the *mycn* mutants (Fig. 5E), and interestingly, ISH of those genes showed that they were all highly enriched in

the developing intestines of the zebrafish embryos (Fig. 5F). Metabolomics analysis also showed abnormal metabolism of multiple amino acids in the *mycn* mutants (Fig. 5G). In summary, these results strongly suggest that the intestinal phenotype in the *mycn* mutants may have been caused by impaired ribosomal machinery and protein translation.

Impaired protein translation was the main cause of the intestinal defects in the mycn mutants

To determine whether ribosomal biogenesis was the main cause of the intestinal defects in the *mycn* mutants, we first conducted a sucrose density-gradient centrifugation assay to investigate the ribosomal profiling in both the mutant and WT embryos at 3 dpf. The amounts of free 40S, 60S, and 80S r-particles and polyribosomes were reduced in the *mycn* mutants (Fig. 6A). This compromised ribosomal biogenesis further slowed down the synthesis of new proteins, as shown by western blotting of a puromycin incorporation assay (Fig. 6B) and immunofluorescence by the anti-puromycin antibody of the intestinal sections (Fig. 6C). Target of rapamycin (TOR) is a highly conserved serine/threonine kinase that regulates protein synthesis in response to various factors, including nutrients, growth factors, and amino acids [32-33]. We then used rapamycin, a TOR inhibitor, to mimic a global protein synthesis defect in the zebrafish embryos. ISH of *ifabp* showed that the increased rapamycin concentration aggravated the intestinal developmental defects (Fig. 6D). These results suggest that proper protein synthesis is essential for intestinal development and that increased protein synthesis may rescue the intestinal defects in *mycn* mutants. Thus, we injected *rheb* mRNA and L-Leu, which can both forcefully activate the TOR pathway, into the *mycn* mutant embryos at 1-cell stage and 30 hpf, respectively. Surprisingly, both L-Leu and Rheb partially rescued the intestinal size in the *mycn* mutant embryos, as shown by *ifabp* expression (Fig. 6E, F). However, although using methotrexate to inhibit purine metabolism led to severe intestinal defects (Fig. S7A), supplementing adenine and guanine in the *mycn* mutants did not restore the intestinal size (Fig. S7B).

Discussion

In this study, we generated *mycn* mutant fish mimicking the symptoms of human Feingold syndrome type 1. Among the many phenotypes caused by Mycn loss of function, we focused on intestinal atresia, a symptom that has the greatest impact on patients' quality of life, yet has an unclear pathogenesis. Our model showed that Mycn plays a direct role in intestinal development by controlling the size of the entire digestive tract by regulating cell proliferation during development. The molecular mechanisms studying revealed that Mycn, as a transcriptional activator, directly regulates the transcription of genes related to ribosomal biosynthesis and assembly.

Importantly, although inhibiting both protein translation and purine metabolism can lead to developmental defects in zebrafish intestines, the intestinal phenotype caused by Mycn loss of function was counteracted only when we used L-Leu or Rheb, which are activators of the TOR signaling pathway, to forcibly elevate the level of protein synthesis. This may provide a potential treatment strategy for alleviating intestinal defects in patients with Feingold syndrome.

Our work showed that during embryonic development, intestinal cells, which are in a highly proliferative state, require high *mycn* expression levels. Interestingly, *mycn* was also highly expressed in the neuroectoderm as early as gastrulation stage and continued to be enriched in the central nervous system during the organogenesis stage. However, we observed no obvious nervous system phenotypes in the *mycn* mutants, either morphologically or from single-cell sequencing. This might be because other MYC family members, such as c-myc or l-myc, which are also expressed in the nervous system, compensate for the function of Mycn. Future double or triple knockout of the Myc family members is required to validate this hypothesis and determine the relationship between the members of the MYC family. Another interesting question raised here is what regulates expression of the Myc genes, and what mechanism achieves the spatiotemporal expression of the Myc family members?

In our *mycn:EGFP* reporter line, *mycn* was expressed in the migrating neuromasts of the lateral line, a sensory organ derived from neural crest cells in zebrafish, and our single-cell transcriptomic data showed that the cell ratios of multiple neural crest-derived organs were significantly lower in the *mycn* mutants. This is somewhat inconsistent with a previous study, which showed that MycN can drive the neural crest toward a neural stem cell-like fate in chicken embryos (6). Based on our single-cell analysis of the *mycn* expression dynamics during development, we hypothesize that *mycn* expression levels might partially affect the fate of neural stem cells and the neural crest. When *mycn* expression is very high, the cells tend to differentiate into neural stem cells, and when the *mycn* expression is lower, the cells become a neural crest. But Mycn is essential for both cell types, and *mycn* deletion does not significantly affect the central nervous system because other Myc family members compensate for it.

Single-cell RNA-seq identified several clusters of developing intestinal cells that were highly sensitive to Mycn loss of function; these clusters were highly proliferating at this developmental stage and thus required a higher amount of *mycn*. Two recent works reported that mitochondrial transcription positively regulates intestinal development [34], and that copper overload affects intestinal development in zebrafish [35]. Among the intestinal clusters from our single-cell data, one cluster (cluster 8) expressing the highest level of *mycn* mRNA completely disappeared in the *mycn* mutants. Interestingly, many marker genes in this cluster are related to mitochondrial function and copper metabolism (Supplementary Table S2), and this cluster may contain the cells that were mainly affected in the aforementioned two works. Our data provide a mechanistic understanding of these phenomena.

In summary, our work generated a zebrafish model of Feingold syndrome type 1. Our results suggest that proliferation arrest caused by protein synthesis blocking was the main reason for the developmental defects in the intestines of *mycn* mutant, suggesting a possible treatment strategy for intestinal symptoms in patients with Feingold syndrome. However, zebrafish were developed in vitro, thus, their nutrient acquisition and developmental environment differ from those of humans, and these results should be validated using a human intestinal organoid system.

Material and methods

Ethics statement

All animal procedures were performed per the requirements of the "Regulation for the Use of Experimental Animals in Zhejiang Province." The Animal Ethics Committee of the School of Medicine, Zhejiang University, approved this study.

Fish lines and maintenance

The zebrafish AB strain was used in all experiments to generate knockin or mutant lines. To generate the *mycn* mutants, we synthesized three gRNAs against the second exon of the zebrafish *mycn* gene as previously described [14]. The Cas9 protein and *mycn*-targeting gRNAs were co-injected into the wild-type (WT) embryos at 1-cell stage. The *mycn* mutant lines were identified in the F1 generation by analyzing the PCR product using the primer pair listed in Supplementary Table S1. To construct *mycn:EGFP* knockin zebrafish, we generated a gRNA targeting the second intron, and a donor DNA with EGFP reporter just before the stop codon of *mycn* flanked with two homologous arms. We co-injected Cas9, gRNA and the donor into zebrafish embryos at the 1-cell stage, then screen embryos with correct EGFP expression.

WISH

Embryos were fixed in 4% paraformaldehyde (PFA) in phosphate-buffered saline (PBS) overnight at 4°C. The probes were labeled with digoxigenin (Roche Diagnostics). The *ifabp*, *lfabp*, *prss1*, *insulin, foxa3, foxa1, gata6, slc15a1b, pyyb, rpls, rps, lmo7a, baiap2l1a, fabp6, id2a, MT-ND2, tcnl, tm4sf4,* and *apoc2* probes were generated and used for WISH as previously described [15]. DNA fragments of above genes were cloned into the pEASY-blunt-zero vector (Transgen), then sequenced. Primers used were listed in Supplementary Table S1.

Paraffin sections, Hematoxylin-eosin (HE) staining, immunofluorescence staining and TUNEL assay

Embryos were fixed in 4% PFA overnight at 4°C for immunofluorescence or HE staining. After washing in PBST (0.1% Tween20 in PBS), the embryos were dehydrated, transparentized with xylene, and mounted in paraffin overnight at 4°C. The sections were cut serially to 3-μm thick and collected on poly-L-lysine-coated glass slides (CITOGLAS, 188105). HE staining was performed using Dyeing and sealing machine (GEMINI AS). Immunofluorescence staining was performed as described [16]. PCNA antibody was purchased from Sigma (P8825, 1:1000); puromycin antibody was purchased from Merck (MABE343, 1:1000). Alexa Fluor 488-labeled secondary antibody (Invitrogen A21206) was used for visualization. The TUNEL assay was performed with the *In Situ* Cell Death Detection Kit (Roche) per the manufacturer's instructions.

Alcian blue staining

The 5 dpf embryos were fixed in 4% PFA at 4°C overnight. The embryos were washed several times with PBS, then stained with 0.1% Alcian blue 8GX in acid alcohol (70% ethanol and 30% glacial acetic acid) overnight at room temperature. After rehydration in PBS, the embryos were digested with 1% trypsin for 1 h at 37°C. Embryos were then washed with PBS several times and stored in glycerol.

Western blot

Proteins of 3 days post-fertilization (dpf) *mycn* mutant and WT zebrafish were harvested in 100 μL RIPA buffer, separately. The protein lysates were separated via SDS-PAGE and transferred to a polyvinylidene difluoride membrane (Millipore). The western blot was performed using anti-puromycin (1:1000, Merck) and anti-mouse-horseradish peroxidase (1:5000, Thermo Fisher, UK). The experiment were carried out for three times.

Sucrose-gradient centrifugations

The sucrose-gradient centrifugations were performed as previously described [17]. WT and *mycn* mutant embryos were collected at 3 dpf, digested with cold 0.5% trypsin to a single-cell suspension, and homogenized in lysis buffer for 20–50 times. The homogenate was centrifuged at 12,000 g for 15 min at 4°C, and the supernatants were layered on top of a 10%–50% sucrose-gradient solution. Ultracentrifugation was performed at 36,000 rpm for 2 hrs (hours) at 4°C. After centrifugation, the absorbance at optical density OD260 of the fractions collected from the top of the tube was detected using a TRAIX detector (Thermo Scientific, USA). The experiment were carried out for twice.

Chemical treatment

2',7'-Dichlorodihydrofluorescein diacetate (DCFH-DA) (5 mg/mL, Sigma) was used to label the zebrafish intestines at 7 dpf. Embryos were treated with DCFH-DA in 0.3X Danieau buffer for 2 hrs. PED6 (D23739, Thermo Fisher) and EnzChek (E6639, Thermo Fisher) were used to test the digestive ability of the intestinal proteins and lipids. Embryos at 7 dpf were treated with 3 μg/mL PED6 or 20 μg/mL EnzChek in a 0.3X Danieau buffer for 3 hrs. Rapamycin was used to inhibit the mTORC1 pathway. Embryos were exposed to 400 and 800 nM rapamycin (Sangon Biotech, China) in a 0.3X Danieau buffer from 10 hpf (hours post fertilization) to 3 dpf. L-Leu and *rheb* mRNA were used to elevate the mTORC1 pathway. Embryos were injected with L-Leu (500 nM, Sigma) at 30 hpf or *rheb* mRNA (100 pg and 150 pg) at 1-cell stage, then harvested at 3 dpf.

Flow cytometry assay

WT and *mycn* mutant embryos with *ET33J1: EGFP* transgenic backgrounds were collected at 3 dpf. For proliferation analysis, the embryos were immersed in 3 mg/mL BrdU in 0.3X Danieau buffer at 60 hpf overnight in the dark, then washed three times with PBST and digested with cold 1% trypsin to a single-cell suspension. The cells were incubated and labeled with BrdU primary antibody and Alexa Fluor 594-labeled secondary antibody. For apoptosis analysis, the cells were stained with the Annexin V-APC/7-AAD apoptosis kit (MultiSciences) per the manufacturer's instructions, and the signal was detected by a DxFLEX flow cytometer. The experiment were carried out for twice.

RNA-seq and GO analysis

WT and *mycn* mutant zebrafish embryos were collected for RNA sequencing at 2 and 3 dpf. Library construction and sequencing were completed by Novogene (Novogene Bioinformatics Technology Co., Ltd., Beijing, China). Paired-end sequencing (Novaseq6000, 150-bp reads) was performed. The sequencing reads were aligned to the zebrafish GRCz11 genome using STAR (https://github.com/alexdobin/STAR) [18], and reads mapped to multiple genomic locations were removed. Gene expression counts for each sample were calculated using featureCounts (Bioinformatics, 30(7):923-30, 2014) [19]. Differential expression analysis was performed using the DESeq2 package (https://github.com/mikelove/DESeq2) [20]. Differentially expressed genes were obtained by comparing the *mycn* mutant to the WT samples with padj ≤0.1 and |log2foldchange| <0. Finally, overlapped down-regulated genes of the 2 and 3 dpf samples were selected. GO biological process analysis was performed with the clusterProfiler package (https://bioconductor.org/packages/clusterProfiler/) [21].

Single-cell RNA-seq library preparation and sequencing

Samples were prepared for the single cell RNA-seq as previously described [22]. Approximately 30 *mycn* mutant or WT zebrafish embryos at 3 dpf were transferred to 1.5mL Low binding microcentrifuge tubes (Eppendorf 022431021). Trypsin-EDTA solution (Beyotime, C0201) was added then the solution was pipetted up and down several times through a P200 tip every 5 min for 30 min. After all embryos were dissociated into single cell, the cells were centrifuged into a pellet and resuspended by adding 200μL 0.05% bovine serum albumin/Ringer's solution. Cell density was quantified manually using hemacytometers (QIUJING Co., Ltd.), and cell viability was analyzed using propidium iodide staining. Libraries were prepared using the Chromium Controller and Chromium Single Cell 3′ Library (10x Genomics, PN-1000074) per the manufacturer's protocol for 10000-cell recovery. Final libraries were sequenced on the Illumina Novaseq6000 (Genergy Bio-technology, Shanghai Co., Ltd.).

Single-cell RNA-seq analysis

Raw sequencing reads were analyzed using the 10X Cellranger pipeline, version 3.0.2, with the default parameters. The expression matrix was obtained after running Cellranger. The R package Seurat (version 4.0.2) [23] was used to perform downstream analysis. We created a Seurat object with the CreateSeuratObject() function with min.cells = 3, min.genes = 100. Next, we performed a standard analysis procedure with the functions FilterCells(), NormalizeData(), FindVariableGenes(), FindClusters(), and FindAllMarkers(), with appropriate parameters. Finally, all clusters were visualized in two dimensions using t-SNE or UMAP. These clusters were annotated based on differentially expressed markers in each cluster or by comparison with published single-cell datasets. The WT and *mycn* mutant datasets were integrated using the Seurat integration procedure. First, variable features for each dataset were normalized and identified independently with nfeatures = 2000. The FindIntegrationAnchors function was used to identify anchors; the anchors were used as input for the IntegrateData function to integrate the two datasets. Finally, the same procedures were performed on the integrated datasets as done for the single dataset with appropriate parameters. The Seurat subset function was used to create an intestinal-cell Seurat object for downstream analysis.

Acknowledgements We thank Dr. Jin-Rong Peng, Dr. Jun Chen and Dr. Ce Gao at Zhejiang University for providing the *ET33J1: EGFP* reporter fish and helpful discussion. We thank Jing-Yao Chen, Qiong Huang and Xiao-Hui Chen from the Morphological Platform and Ying-Niang Li from the zebrafish core facility at Zhejiang University School of Medicine for their technical support. We thank Guang-Xu Zhang at the Accuramed Technology (Shanghai) Limited for his technical support. We thank Shao-Ge Luo at the Third Affiliated Hospital, Sun Yat-Sen University for his technical help.

Compliance with ethical standards

Conflict of interest The authors declare that they have no conflict of interest.

Publisher's note Springer Nature remains neutral with regard to jurisdictional claims in published maps and institutional affiliations.

References

1. Mirzamohammadi, F, Kozlova, A, Papaioannou, G, Paltrinieri, E, Ayturk, UM and Kobayashi, T, (2018) Distinct molecular pathways mediate Mycn and Myc-regulated miR-17-92 microRNA action in Feingold syndrome mouse models. Nat Commun 9: 1352.

2. Teszas, A, Meijer, R, Scheffer, H, Gyuris, P, Kosztolanyi, G and van Bokhoven, H *et al.*, (2006) Expanding the clinical spectrum of MYCN-related Feingold syndrome. Am J Med Genet A 140: 2254-6.

3. Richards, MW, Burgess, SG, Poon, E, Carstensen, A, Eilers, M and Chesler, L *et al.*, (2016) Structural basis of N-Myc binding by Aurora-A and its destabilization by kinase inhibitors. Proc Natl Acad Sci U S A 113: 13726-13731.

4. Beltran, H, (2014) The N-myc Oncogene: Maximizing its Targets, Regulation, and Therapeutic Potential. Mol Cancer Res 12: 815-22.

5. Lasorella, A, Noseda, M, Beyna, M, Yokota, Y and Iavarone, A, (2000) Id2 is a retinoblastoma protein target and mediates signalling by Myc oncoproteins. Nature 407: 592-8.

6. Kerosuo, L, Neppala, P, Hsin, J, Mohlin, S, Vieceli, FM and Torok, Z *et al.*, (2018) Enhanced expression of MycN/CIP2A drives neural crest toward a neural stem cell-like fate: Implications for priming of neuroblastoma. Proc Natl Acad Sci U S A 115: E7351-E7360.

7. Stanton, BR, Perkins, AS, Tessarollo, L, Sassoon, DA and Parada, LF, (1992) Loss of N-myc function results in embryonic lethality and failure of the epithelial component of the embryo to develop. Genes Dev 6: 2235-47.

8. Knoepfler, PS, Cheng, PF and Eisenman, RN, (2002) N-myc is essential during neurogenesis for the rapid expansion of progenitor cell populations and the inhibition of neuronal differentiation. Genes Dev 16: 2699-712.

9. Wells, JM and Melton, DA, (1999) Vertebrate endoderm development. Annu Rev Cell Dev Biol 15: 393-410.

10. Zhao, X and Pack, M, (2017) Modeling intestinal disorders using zebrafish. Methods Cell Biol 138: 241-270.

11. Wallace, KN, Akhter, S, Smith, EM, Lorent, K and Pack, M, (2005) Intestinal growth and differentiation in zebrafish. Mech Dev 122: 157-73.

12. Qiao, R, Sheng, C, Lu, Y, Zhang, Y, Ren, H and Lemos, B, (2019) Microplastics induce intestinal inflammation, oxidative stress, and disorders of metabolome and microbiome in zebrafish. Sci Total Environ 662: 246-253.

13. Xie, Y, Meijer, AH and Schaaf, M, (2020) Modeling Inflammation in Zebrafish for the Development of Anti-inflammatory Drugs. Front Cell Dev Biol 8: 620984.

14. Chang, N, Sun, C, Gao, L, Zhu, D, Xu, X and Zhu, X *et al.*, (2013) Genome editing with RNA-guided Cas9 nuclease in zebrafish embryos. Cell Res 23: 465-72.

15. Thisse, B and Thisse, C, (2014) In situ hybridization on whole-mount zebrafish embryos and young larvae. Methods Mol Biol 1211: 53-67.

16. van Boxtel, AL, Chesebro, JE, Heliot, C, Ramel, MC, Stone, RK and Hill, CS, (2015) A Temporal Window for Signal Activation Dictates the Dimensions of a Nodal Signaling Domain. Dev Cell 35: 175-85.

17. Lu, H, Ma, J, Yang, Y, Shi, W and Luo, L, (2013) EpCAM is an endoderm-specific Wnt derepressor that licenses hepatic development. Dev Cell 24: 543-53.

18. Dobin, A, Davis, CA, Schlesinger, F, Drenkow, J, Zaleski, C and Jha, S *et al.*, (2013) STAR: ultrafast universal RNA-seq aligner. Bioinformatics 29: 15-21.

19. Liao, Y, Smyth, GK and Shi, W, (2014) featureCounts: an efficient general purpose program for assigning sequence reads to genomic features. Bioinformatics 30: 923-30.

20. Love, MI, Huber, W and Anders, S, (2014) Moderated estimation of fold change and dispersion for RNA-seq data with DESeq2. Genome Biol 15: 550.

21. Yu, G, Wang, LG, Han, Y and He, QY, (2012) clusterProfiler: an R package for comparing biological themes among gene clusters. OMICS 16: 284-7.

22. Cheng, T, Xing, Y, Li, Y, Liu, C, Huang, Y and Zhang, Y *et al.*, (2021) Single cell response landscape of graded Nodal signaling in zebrafish explants. bioRxiv: 2021.04.25.441305.

23. Hao, Y, Hao, S, Andersen-Nissen, E, Mauck, WR, Zheng, S and Butler, A *et al.*, (2021) Integrated analysis of multimodal single-cell data. Cell 184: 3573-3587.e29.

24. Otte, J, Dyberg, C, Pepich, A and Johnsen, JI, (2020) MYCN Function in Neuroblastoma Development. Front Oncol 10: 624079.

25. Farnsworth, DR, Saunders, LM and Miller, AC, (2020) A single-cell transcriptome atlas for zebrafish development. Dev Biol 459: 100-108.

26. Wagner, DE, Weinreb, C, Collins, ZM, Briggs, JA, Megason, SG and Klein, AM, (2018) Single-cell mapping of gene expression landscapes and lineage in the zebrafish embryo. Science 360: 981-987.

27. Farrell, JA, Wang, Y, Riesenfeld, SJ, Shekhar, K, Regev, A and Schier, AF, (2018) Single-cell reconstruction of developmental trajectories during zebrafish embryogenesis. Science 360.

28. Gao, C, Huang, W, Gao, Y, Lo, LJ, Luo, L and Huang, H *et al.*, (2019) Zebrafish hhex-null mutant develops an intrahepatic intestinal tube due to de-repression of cdx1b and pdx1. J Mol Cell Biol 11: 448-462.

29. Zhao, S, Xia, J, Wu, X, Zhang, L, Wang, P and Wang, H *et al.*, (2018) Deficiency in class III PI3-kinase confers postnatal lethality with IBD-like features in zebrafish. Nat Commun 9: 2639.

30. Ng, AN, de Jong-Curtain, TA, Mawdsley, DJ, White, SJ, Shin, J and Appel, B *et al.*, (2005) Formation of the digestive system in zebrafish: III. Intestinal epithelium morphogenesis. Dev Biol 286: 114-35.

31. Chen, X, Xu, H, Yuan, P, Fang, F, Huss, M and Vega, VB *et al.*, (2008) Integration of external signaling pathways with the core transcriptional network in embryonic stem cells. Cell 133: 1106-17.

32. Hua, H, Kong, Q, Zhang, H, Wang, J, Luo, T and Jiang, Y, (2019) Targeting mTOR for cancer therapy. J Hematol Oncol 12: 71.

33. You, JS, Anderson, GB, Dooley, MS and Hornberger, TA, (2015) The role of mTOR signaling in the regulation of protein synthesis and muscle mass during immobilization in mice. Dis Model Mech 8: 1059-69.

34. Peron, M, Dinarello, A, Meneghetti, G, Martorano, L, Betto, RM and Facchinello, N *et al.*, (2021) Y705 and S727 are required for the mitochondrial import and transcriptional activities of STAT3, and for regulation of stem cell proliferation. Development 148.

35. Zhao, G, Zhang, T, Sun, H and Liu, JX, (2020) Copper nanoparticles induce zebrafish intestinal defects via endoplasmic reticulum and oxidative stress. Metallomics 12: 12-22.

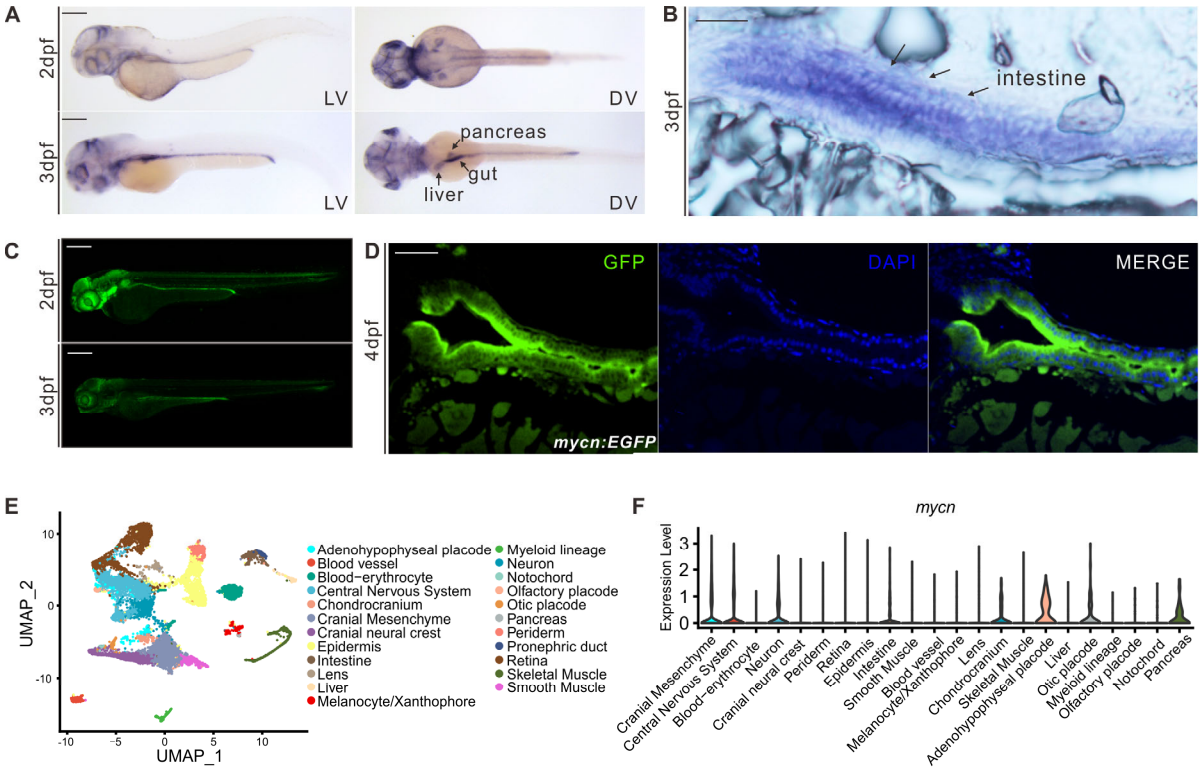

Fig. 1. *mycn* expression patterns in zebrafish during early development. A Expression patterns of *mycn* in zebrafish at 2 and 3 dpf by whole-mount WISH. Lateral view (left), dorsal view (right). **B** *mycn* expressed along the whole intestines of the embryos at 3 dpf shown by section via ISH. Arrows indicate the embryo intestines. Sections were cut along the sagittal plane. **C** Fluorescence images show the *mycn* expression patterns by EGFP-knockin fish at 2 and 3 dpf (lateral view). **D** *mycn* expressed along the whole intestines of the zebrafish at 4 dpf shown by section of *mycn:EGFP* fish. **E** Uniform manifold approximation and projection (UMAP) plot shows unsupervised clustering of the cells in wild-type embryos of 3 dpf; cells are colored by their cell-type annotations. **F** Violin plots show the *mycn* expression levels of different cell types of wild-type embryonic scRNA-seq data at 3 dpf. Scale bars: 200 μm (A and C), 50 μm (B and D).

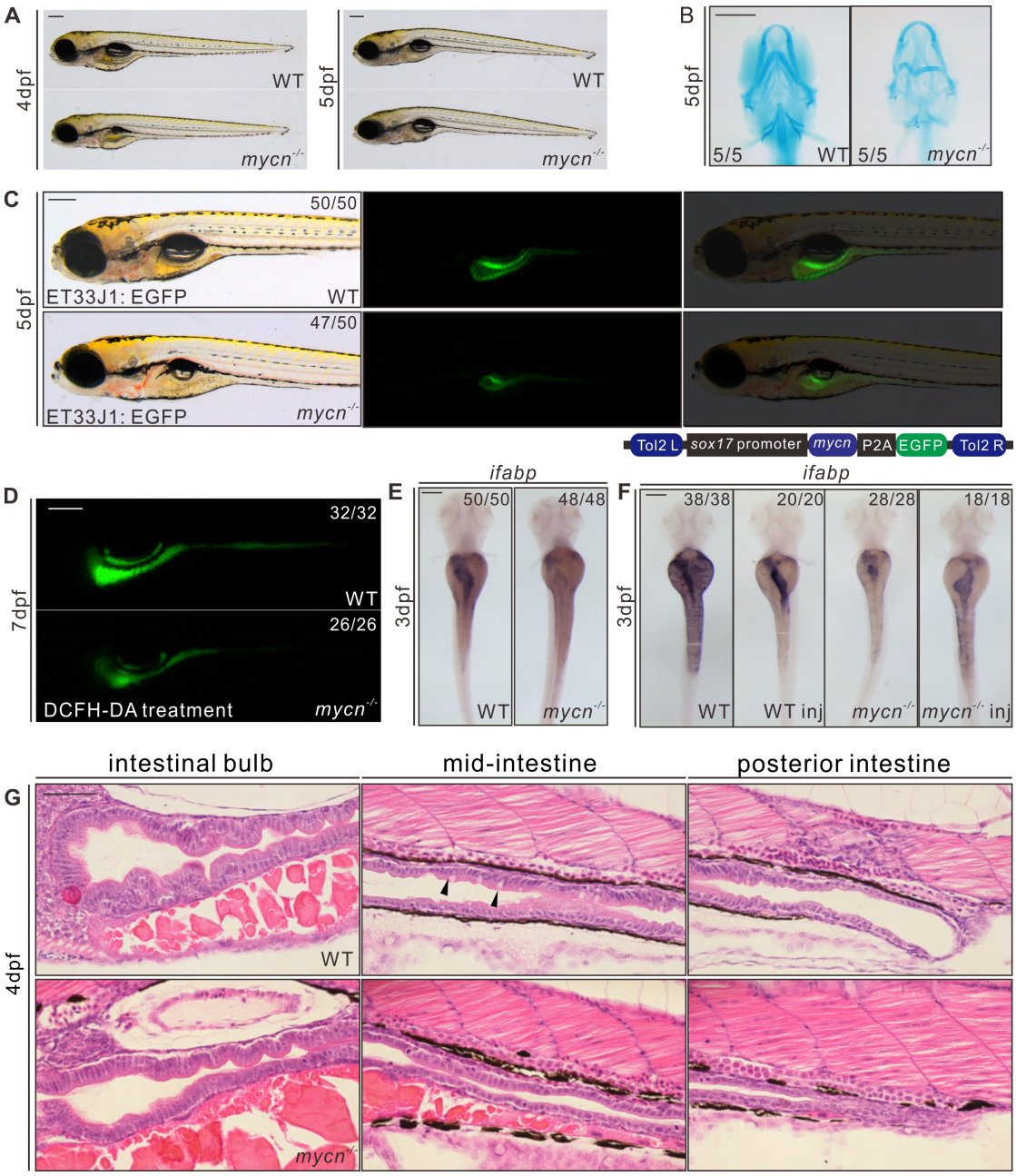

Fig. 2. Phenotypic analysis of *mycn* mutants. A Bright-field images show that the *mycn* mutants lacked swim bladder at 4 dpf, but appeared at 5 dpf. All embryos are shown in lateral view. **B** Abnormal pharyngeal arch development was observed in *mycn* mutants via Alcian blue staining; images show the head region of wild-type and mycn mutant embryos at 5 dpf (ventral view). **C** Intestinal lumens in wild-type and *mycn* mutant embryos at 5 dpf shown by *ET33J1: EGFP* reporter (Lateral view). **D** Fluorescence signals show the morphology of the whole intestines in wild-type and *mycn* mutant embryos at 7 dpf via DCFH-DA treatment (lateral view). **E** Expression of *ifabp* by WISH showing intestines in wild-type and *mycn* mutant embryos at 3 dpf (dorsal view). **F** Expression of *ifabp* in WT (two images on the left) and *mycn* mutant embryos (two images on the right) at 3 dpf. Overexpression of *mycn* specifically in endoderm cells via injection of a plasmid in which the *mycn* expression was driven by *sox17* promoter (diagram of the construct shown on the top); the injected embryos are labeled with "inj" at the bottom of the image. **G** Morphology of the whole intestine visualized via hematoxylin-

eosin staining for the wild-type and *mycn* mutant embryo sections at 4 dpf. Black arrows indicate goblet cells in the wild-type intestines. Sections were cut along the sagittal plane. Scale bars: 200 μm (A-F), 50 μm (G).

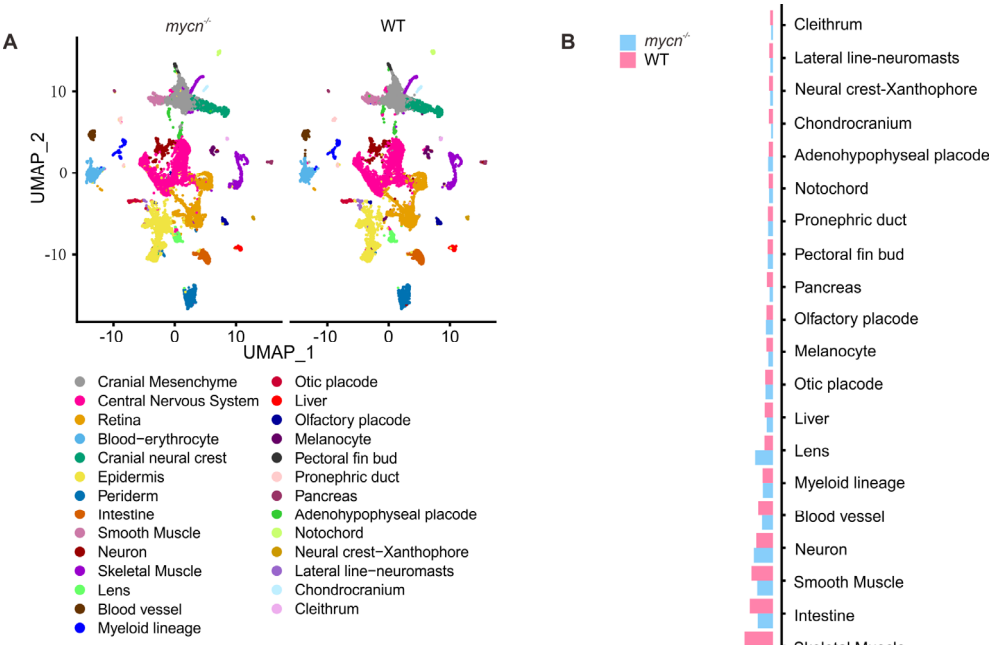

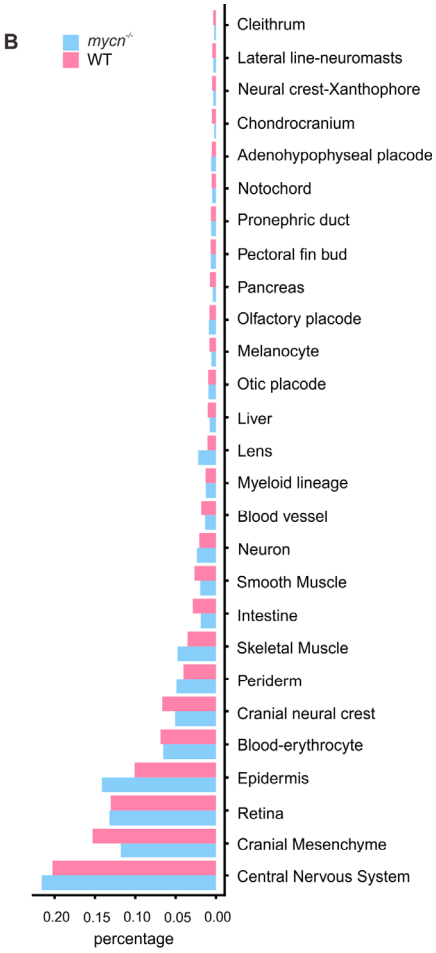

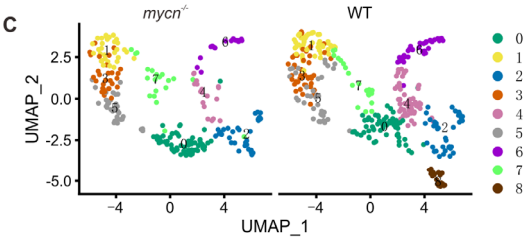

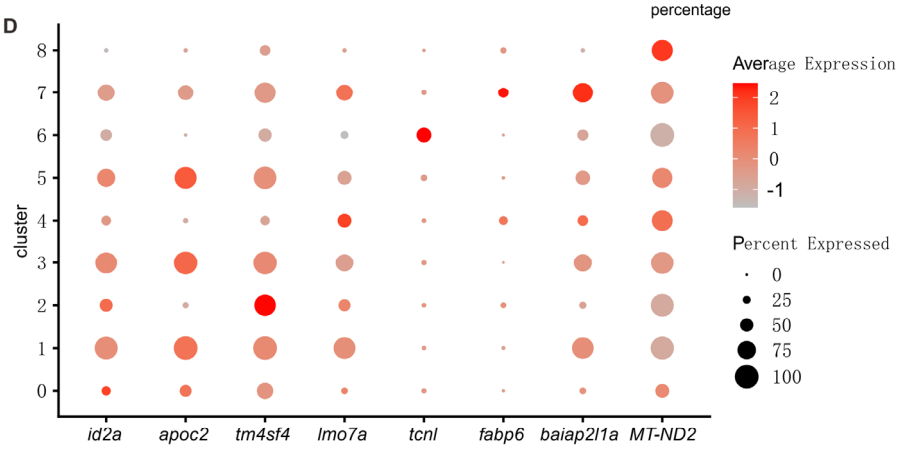

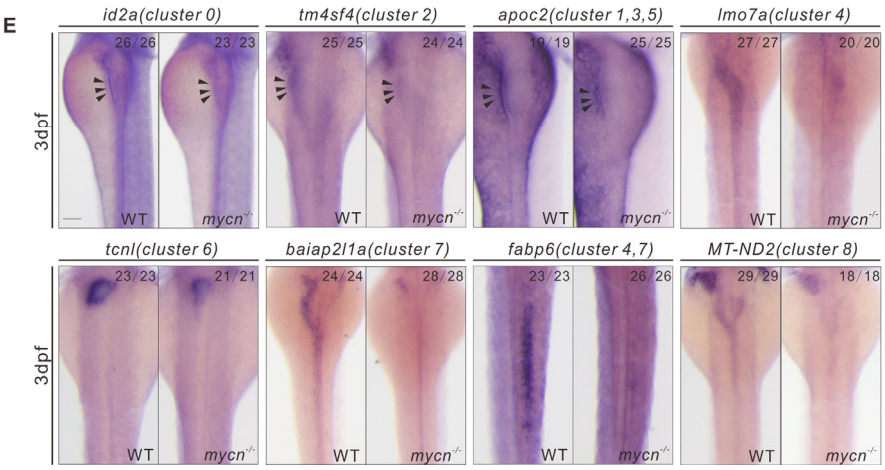

Fig. 3. Single cell RNA-seq analysis of wild-type and *mycn* mutant embryos at 3 dpf. A Unsupervised clustering of cells in the *mycn* mutants and wild-type embryos at 3 dpf. Cells are colored according to their cell-type annotations inferred from expressed marker genes and published datasets. **B** Bar plot shows the percentages of each cell type in *mycn* mutants (blue) or wild-type embryos (red). **C** UMAP plot shows the subclusters of intestinal cells selected from A. Cells are colored by cell-type clusters. 9 clusters were identified by unsupervised clustering. **D** Dot plot shows the expressions of marker genes in each subcluster of intestinal cells. Heatmap represents average expression level and dot size represents percentage of cell expression across *mycn* mutant and wild-type embryos. **E** WISH results show the expression of marker genes of each cluster: *id2a* (cluster 0), *tm4sf4* (cluster 2), *apoc2* (clusters 1, 3, 5), *lmo7a* (cluster 4), *tcnl* (cluster 6), *baiap2l1a* (cluster 7), *fabp6* (clusters 4, 7), MT-ND2 (cluster 8) in wild-type and *mycn* mutant embryos. Arrow heads indicate the intestines. Scale bar: 100 μm.

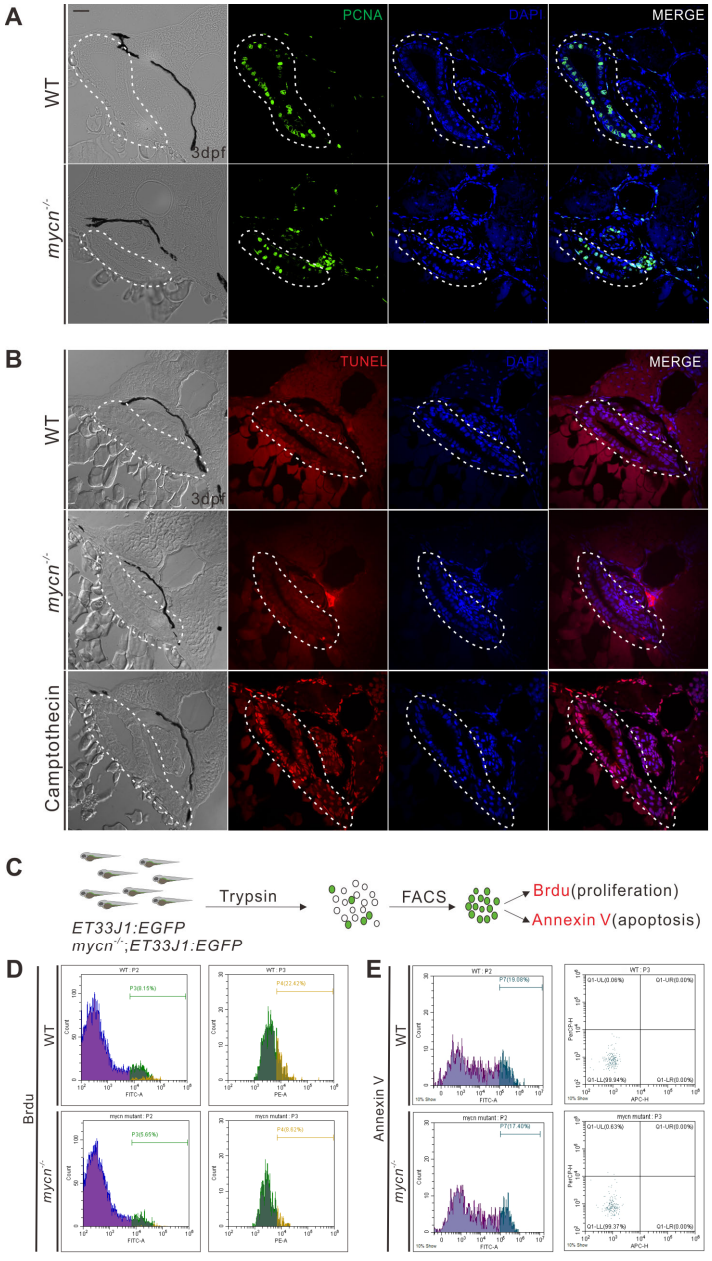

Fig. 4. Detection of cell proliferation and apoptosis in intestines of wild-type and *mycn* mutant. A Cell proliferation in the intestines was detected by proliferating-cell nuclear antigen (PCNA) immunofluorescence staining (green signal) of the tissue sections from the wild-type and *mycn* mutant embryos. **B Apoptosis** in the intestines was detected via TUNEL assay (red signal) for the tissue sections from the wild-type, *mycn*-mutant, and camptothecin-treated (as positive control) embryos. Sections were cut along the transverse plane. Dotted lines indicate the intestine positions. **C** Schematic representation of the experimental workflow of the flow cytometry analysis. **D** Cell proliferation in the intestines was detected by BrdU incorporation assay. **E** Apoptosis in the intestines was detected by APC-Annexin V staining. Embryos used in the flow cytometry analysis were descendants of *ET33J1:EGFP* reporter line crossed with wild-type or *mycn* mutants (D and E). Scale bar: 50 μm.

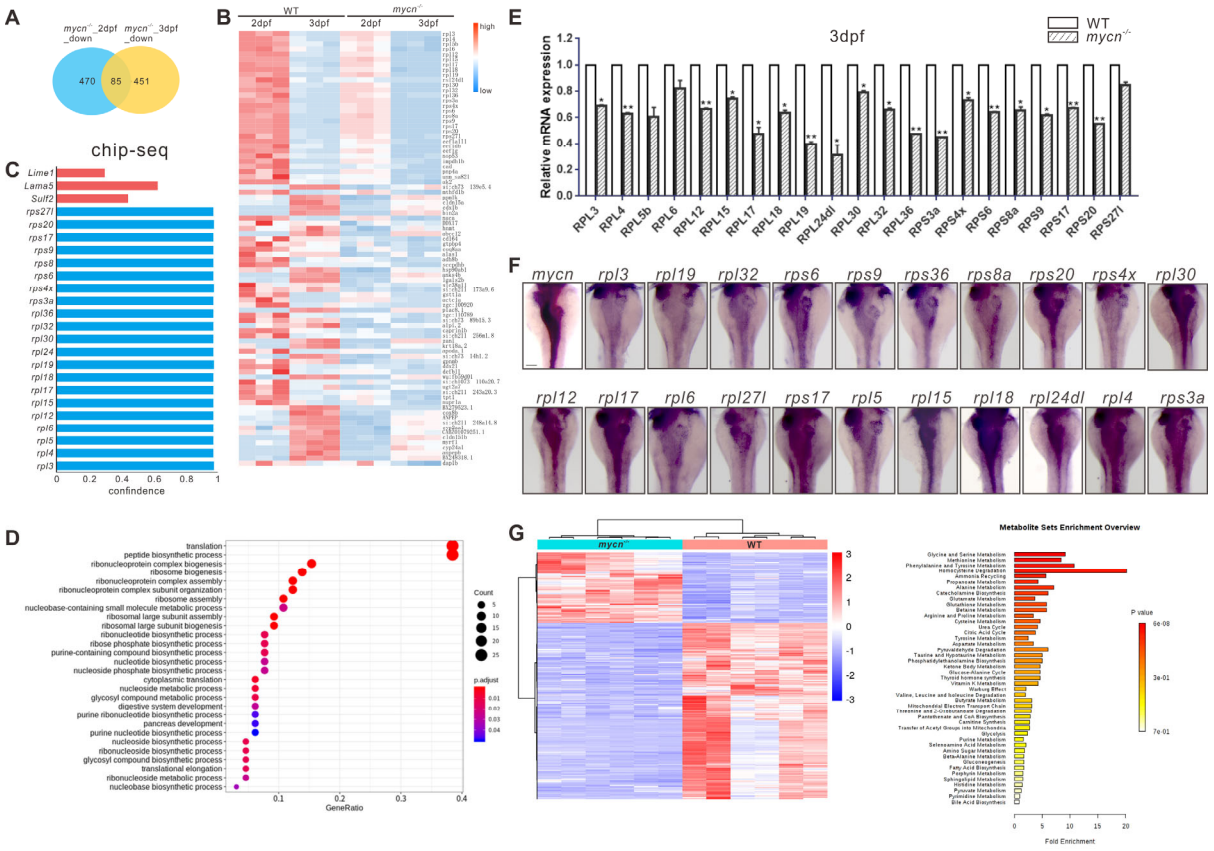

Fig. 5. Multi-omics analysis in the *mycn* mutant and wild-type embryos. A Venn diagram of the downregulated genes in *mycn* mutants compared with wild-type at 2 and 3 dpf. The number of congruently downregulated genes is showed in the middle. **B** Heatmap showing the scaled expression patterns of 85 downregulated genes (identified in A) in *mycn* mutant and wild-type embryos at 2 and 3 dpf. Color scale: red, high expression; blue, low expression. **C** Bar plot shows the confidence interval of a portion of the *rpl* and *rps* genes that were direct downstream targets of MYCN analyzed by ChIP-seq of *MYCN* in the mouse ESC from published datasets (31). These genes were also been found downregulated in the *mycn* mutants by bulk RNA-seq analysis. **D** Dot plot showing enriched GO terms of the 85 downregulated genes in the *mycn* mutants. The size and color intensity of each dot represents the gene counts in each enriched GO term and the adjusted *p*-value, respectively. **E** qPCR verification of the downregulated *rpl* and *rps* genes at 3 dpf in wild-type and *mycn*

mutant embryos. Asterisks indicate that the significant difference by Student's *t*-test. $^{**}p < 0.001$; $^{*}p < 0.05$. **F** Expression patterns of *rpl* and *rps* genes and *mycn* in the digestive organs of wild-type embryos at 3 dpf via WISH (images shown in dorsal view). **G** Metabolite analysis of the *mycn* mutant and wild-type embryos. The heatmap shows the expressions of different substances in *mycn* mutant and wild-type embryos after normalizing the intensity value of each metabolite. Bar plot shows the KEGG pathway enrichment and enrichment significance calculated by analysis of differential metabolites between the *mycn* mutant and wild-type embryos. Fold enrichment is the ratio of the number of metabolites matching the pathway during enrichment analysis to the number of theoretical metabolites distributed to the pathway of random distribution. Enrichment significance is indicated by color in the histogram according to *p*-value. Scale bar: 100 μm.

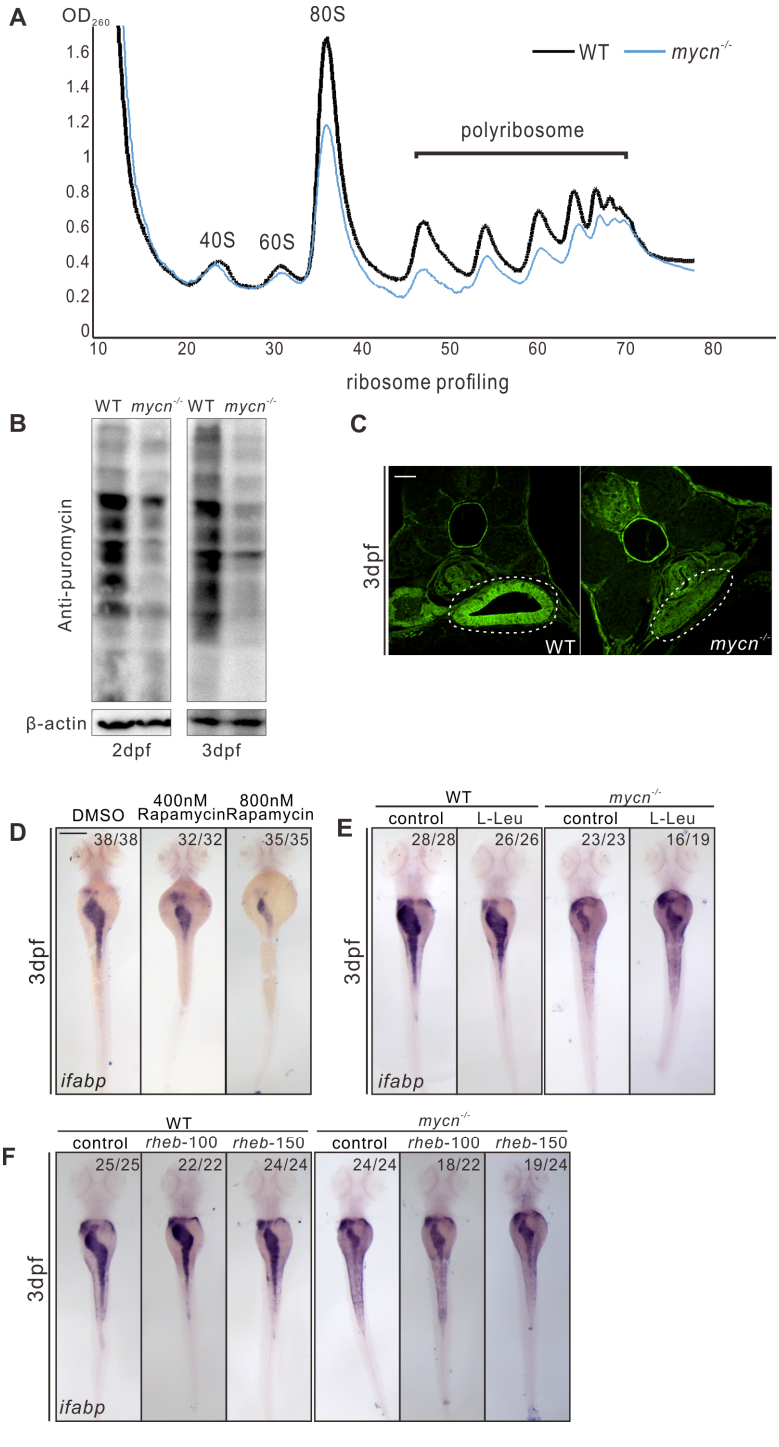

Fig. 6. Impaired protein translation results to intestinal defects in *mycn* mutants.

A Ribosomal profiling of *mycn* mutant and wild-type embryos at 3 dpf was performed by sucrose density-gradient centrifugation. All samples were normalized by the total RNA. **B** Detection of nascent protein synthesis by puromycin incorporation assay in wild-type and *mycn* mutant embryos at 2 and 3 dpf. Puromycin-incorporated neosynthesized proteins were detected by western blot with anti-puromycin antibody. The β-actin expression level was used as internal control. **C** Nascent protein synthesis was detected by section immunofluorescence with anti-puromycin antibody in wild-type and *mycn* mutant embryos at 3 dpf. Sections were cut along the transverse plane. **D** Inhibiting the mTOR pathway by different doses of rapamycin mimicked the intestinal-defects phenotype of the *mycn* mutants. **E** Activating the mTOR pathway by L-Leu treatment partially rescued the intestinal-defects phenotype of the *mycn* mutants. **F** Activating the mTOR pathway by injecting *rheb* mRNA partially rescued the intestinal-defects phenotype of the *mycn* mutants. All embryos are shown in dorsal view. Scale bar: 50 μm C, 200 μm (D-F).